



Publication Year	2018
Acceptance in OA	2020-10-16T15:52:43Z
Title	Fast deuterium fractionation in magnetized and turbulent filaments
Authors	Körtgen, B., Bovino, S., Schleicher, D. R. G., Stutz, A., Banerjee, R., GIANNETTI, ANDREA, Leurini, Silvia
Publisher's version (DOI)	10.1093/mnras/sty993
Handle	http://hdl.handle.net/20.500.12386/27864
Journal	MONTHLY NOTICES OF THE ROYAL ASTRONOMICAL SOCIETY
Volume	478

Fast deuterium fractionation in magnetized and turbulent filaments

B. Körtgen,¹★ S. Bovino,² D. R. G. Schleicher,² A. Stutz,² R. Banerjee,¹ A. Giannetti³ and S. Leurini⁴

¹Hamburger Sternwarte, Universität Hamburg, Gojenbergsweg 112, D-21029 Hamburg, Germany

²Departamento de Astronomía, Facultad Ciencias Físicas y Matemáticas, Universidad de Concepción, Av. Esteban Iturra s/n Barrio Universitario, Casilla 160-C, Concepción, Chile

³INAF – Istituto di Radioastronomia & Italian ALMA Regional Centre, Via P. Gobetti 101, I-40129 Bologna, Italy

⁴INAF Osservatorio Astronomico di Cagliari, Via della Scienza 5, I-09047 Selargius, Italy

Accepted 2018 April 11. Received 2018 April 6; in original form 2017 September 11

ABSTRACT

Deuterium fractionation is considered as an important process to infer the chemical ages of prestellar cores in filaments. We present here the first magnetohydrodynamical simulations including a chemical network to study deuterium fractionation in magnetized and turbulent filaments, with a line-mass of $M_{\text{lin}} = 42 M_{\odot} \text{pc}^{-1}$ within a radius of $R = 0.1 \text{ pc}$, and their sub-structures. The filaments typically show widespread deuterium fractionation with average values $\gtrsim 0.01$. For individual cores of similar age, we observe the deuteration fraction to increase with time, but also to be independent of their average properties such as density, virial, or mass-to-magnetic flux ratio. We further find a correlation of the deuteration fraction with core mass, average H_2 density, and virial parameter only at late evolutionary stages of the filament and attribute this to the lifetime of the individual cores. Specifically, chemically old cores reveal higher deuteration fractions. Within the radial profiles of selected cores, we notice differences in the structure of the deuteration fraction or surface density, which we can attribute to their different turbulent properties. High deuteration fractions of the order of 0.01–0.1 may be reached within approximately 200 kyr, corresponding to two free-fall times, as defined for cylindrical systems, of the filaments.

Key words: astrochemistry – magnetic fields – MHD – turbulence – stars: formation – ISM: clouds.

1 INTRODUCTION

Filamentary structures have been known since the time of Barnard (1905)¹ through the discovery on photographic plate data. Their ubiquitous presence inside molecular clouds has been most recently revealed by surveys such as the Herschel Gould Belt Survey (André et al. 2010), the Herschel Hi-GAL Milky Way survey (Molinari et al. 2010), or the characterization of filaments in IC 5147 (Arzoumanian et al. 2011). The physics of such filaments under conditions of equilibrium was initially described by Chandrasekhar & Fermi (1953), taking into account gravity, thermal pressure, rotation, and magnetic fields. These investigations have been extended by various authors, including Nagasawa (1987), Fiege & Pudritz (2000), Tomisaka (2014), and Toci & Galli (2015). As most of star formation occurs in filaments (André et al. 2014; Stutz & Gould 2016), it is thus particularly important to understand their general properties

as well as their stability and how they first fragment into larger clumps and subsequently into cores.

The observed star formation rate and efficiency have been measured for many filaments with various properties and within different environments (see e.g. review by André et al. 2014) and the question was posed how filaments with suppressed star formation can be stabilized against (radial) contraction. In this sense, the impact of different types of magnetic field structures was predominantly explored via linear stability analysis, with very early studies initially focusing on axial or helical fields (Nakamura et al. 1993; Matsumoto et al. 1994; Fiege & Pudritz 2000), while more recently also perpendicular field structures were considered by Hanawa & Tomisaka (2015). As a central result, they found that filaments cannot be stabilized against fragmentation by axial magnetic fields, while perpendicular ones can have a relevant stabilizing contribution.

Polarimetry observations suggest a bi-modal distribution of magnetic field alignment with the filament (Li et al. 2013), and more recent results suggest a lower specific star formation rate in the case of perpendicular magnetic fields (Li et al. 2017). The result is thus

* E-mail: bkoertgen@hs.uni-hamburg.de

¹See http://www.library.gatech.edu/Barnard_Project_W/PDF/plate41.pdf.

in line with expectations based on linear theory. Numerical simulations by Seifried & Walch (2015) however show that axial fields can at least stabilize the filaments along the radial direction, leading to a reduced number of stars in their simulations. More recently, Seifried & Walch (2016) carried out high-resolution numerical simulations including a complex chemical network to study the evolution of filaments. They find strong chemical differentiation (i.e. chemical gradients) throughout the filament. Post-processing these data and generating synthetic observations, Seifried et al. (2017) found that the general properties of their simulated filaments (such as their mass or width) can be probed more accurately via dust emission, but line emission observations seem to fail to reproduce the properties of the filaments directly extracted from the simulations. The authors state that e.g. the assumption of a constant excitation temperature introduces errors as it does not account for strong variations in the gas temperature along the line of sight.

The collapse and fragmentation of filaments have been studied intensively from a numerical point of view. Burkert & Hartmann (2004) have shown via 2D simulations that there appears to be a preferred edge-on (starting at the end points) fragmentation of filaments, which is independent of the initial conditions. They further emphasize that a degree of inhomogeneity of the filament surface may indeed help to drive turbulence within the filament. More recently Clarke & Whitworth (2015) have shown that this edge-on mode of fragmentation happens for all filaments with aspect ratios $\gtrsim 2$ and that the resulting fragments greatly influence the gas inside the filaments. A similar study by Seifried & Walch (2015) reveals that filament fragmentation can be either edge-on, centralised or both, primarily depending on the initial ratio of the filament line-mass to the critical one.

Observationally, the fragmentation of filaments was analysed by Hacar & Tafalla (2011, see also Hacar et al. 2013), finding that pc-scale filaments fragment into small-scale, velocity-coherent structures, which can then undergo fragmentation to form individual cores. These ‘fibres’ are closely linked to the vorticity in the filament, as has been suggested recently by Clarke et al. (2017). In addition, velocity gradients across cores have been found in the infrared dark cloud G351.77-051 by Leurini et al. (2011). These gradients were assigned to CO outflows, which indicate past fragmentation and active star formation. Furthermore, in the Orion A cloud, where the combination of polarimetry and Zeeman measurements shows evidence for a helical field (Heiles 1987; Bally 1989; Heiles 1997; Pattle et al. 2017), recent measurements suggest approximate equipartition between gravitational and magnetic energy on 1 pc scales, as well as potential oscillations and instabilities induced by magnetic fields (Stutz & Gould 2016), giving rise to the possible influence of large-scale environmental effects on the fragmentation of filaments. The potential oscillation is consistent with analytic estimates regarding the impact of helical fields (Schleicher & Stutz 2018) as well as with stellar dynamical calculations (Boekholt et al. 2017).

Strong controversies are however still present regarding the way stars form in gravitationally unstable cores, in particular high-mass stars. Whether it happens on approximately a free-fall time, as suggested in the competitive accretion scenario by Bonnell et al. (2001), or rather slowly, implying at least several free-fall times, in the core accretion model by McKee & Tan (2003), which assumes that turbulence and/or magnetic fields provide a major stabilizing contribution. It is therefore of central importance to obtain independent constraints on the time-scale of star formation. A potentially powerful tool that was suggested in the literature is the measurement of deuteration fractions, which may be translated into time-

scales via chemical models (Caselli et al. 2002; Fontani et al. 2011; Pagani et al. 2011a; Kong et al. 2015; Barnes et al. 2016; Lackington et al. 2016). In relation to filaments, a time-scale estimate has recently been achieved by Lackington et al. (2016) for the infrared dark cloud L332. They found deuteration ratios N_2D^+/N_2H^+ in the range 0.003–0.14. Based on the chemical models by Kong et al. (2015), the authors deduced time-scales for various cores within L332 of the order of several free-fall times to match the observed deuteration fractions, indicating rather old cores. The free-fall time of their best-fitting model was $t_{\text{ff}} = 1.39 \times 10^5$ yr at a density of $n_H = 10^5 \text{ cm}^{-3}$. However, the authors emphasize that a change in the CO depletion factor reduces the time-scale to only one free-fall time, which points towards (dynamically) young objects. In addition, Barnes et al. (2016) deduce a chemical age of about eight free-fall times (defined for spherical systems at a density of $n = 10^4 \text{ cm}^{-3}$, giving $t_{\text{ff}} = 3.4 \times 10^5$ yr) for the dark cloud G035.39-00.33 to fit the observed average deuteration fraction of 0.04 ± 0.01 , which they attribute to support of the filament by magnetic fields and turbulence. Furthermore, these authors find that deuteration is widespread over the filament rather than concentrated in individual cores, in agreement with recent findings by Pillai et al. (2012) who report widespread H_2D^+ emission in Cygnus X.

To test how reliably deuterium fractionation can be used as a chemical clock requires numerical simulations, which investigate the build-up of high deuteration under realistic conditions. A first set of 3D magnetohydrodynamical simulations of collapsing cores has been exploited by Goodson et al. (2016), who determined effective formation rates of deuterated species from detailed one-zone models, finding that observed fractions of up to 0.1 can be reproduced after a time, which corresponds to 3–4 times the initial free-fall time of the simulated core, where $t_{\text{ff,initial}} = 7.6 \times 10^4$ yr. Employing the chemical network by Walmsley et al. (2004), which has been fully coupled to the 3D magnetohydrodynamics (MHD) code FLASH, Körtgen et al. (2017) have shown that rapid deuteration occurs within roughly one free-fall time, where the free-fall time was defined by using the average initial core density. These models assumed full depletion, which is in line with previous numerical models and observational measurements, which give high depletion factors already at densities of about 10^4 cm^{-3} (e.g. Chen et al. 2011; Hernandez et al. 2011; Giannetti et al. 2014; Hocuk et al. 2014).

However, to further test this scenario, deuterium fractionation must be explored in a broader context. Particularly, models that follow the collapse of individual cores need pre-determined initial conditions, which are not known from observations. This is particularly true for the ortho-to-para ratio of molecular hydrogen, which plays a crucial role in the deuterium fractionation (e.g. Walmsley et al. 2004; Bovino et al. 2017). A discussion of the limits of the ortho-to-para ratio in comparison with observations of prestellar cores and infrared dark clouds can be found in Pagani et al. (2011b, 2013). Here, we therefore investigate deuterium fractionation on the scale of a filament, focusing on the global chemical evolution as well as the properties of individual cores within the filament. Our numerical method and initial conditions are described in Section 2, and the results are outlined in Section 3. In Section 4, we compare our results to previous lower dimensional studies of deuterium fractionation. A summary with our main conclusions is given in Section 5.

2 NUMERICAL MODEL

We describe here the numerical method employed, the filament setup as well as the chemical network and its initial conditions.

2.1 Method

We use the FLASH code (v4.2.2) to solve the MHD equations as well as the Poisson equation for self-gravity (Fryxell et al. 2000; Dubey et al. 2008). The (magneto)hydrodynamical system is solved with a HLL5R-solver, which preserves positivity of density and internal energy (Bouchut et al. 2010; Waagan et al. 2011), while we use a tree-solver for the self-gravity (optimized for GPU, Lukat & Banerjee 2016). We further employ outflow boundary conditions for the hydrodynamics and isolated ones for the self-gravity. Gravitationally collapsing regions with increasing density are replaced by a Lagrangian sink particle to avoid violation of the Truelove criterion (Truelove et al. 1997). Besides other tests of gravitational stability (see Federrath et al. 2010), the grid cells have to exceed a threshold density of $n_{\text{thresh}} = 8 \times 10^7 \text{ cm}^{-3}$ before a sink particle is formed. We anticipate here that no sink particles form in the simulations as most of the formation criteria are not fulfilled.

The size of the numerical domain is $L_{\text{box}} = 6 \text{ pc}$ in each direction. We allow a maximum refinement level of 13, corresponding to a minimum cell size of $\Delta x = 147 \text{ au}$. The numerical grid is refined once the local Jeans length is resolved with less than 16 cells. In addition, the Jeans length at the threshold density is still refined with eight grid cells, which shows that this density is still numerically resolved.

The FLASH code is coupled to the astrochemistry package KROME² (Grassi et al. 2014), employing the high-order solver DLSODES for solving the chemical rate equations. The chemical initial conditions and the network are described further below.

2.2 Initial filament properties and dynamics

Recent observational surveys (with e.g. *Herschel*) have revealed that interstellar filaments appear to be rather similar in their properties, such as e.g. their spatial distribution of the gas in the radial direction, though these findings have been questioned (e.g. Juvela et al. 2012). As was shown by Arzoumanian et al. (2011), the radial density profile of observed filaments is best fitted with a Plummer-like distribution:

$$\rho(R) = \frac{\rho_{\text{ridge}}}{\{1 + (R/R_{\text{flat}})^2\}^{p/2}}. \quad (1)$$

Here ρ_{ridge} is the central density, R is the radius, R_{flat} the characteristic width of the flat inner plateau of the filament, and p is the typical exponent of the profile, respectively. Arzoumanian et al. (2011) give values $1.5 < p < 2.5$ for the profile exponent and a typical filament width $\sim 3 \times R_{\text{flat}}$ with $0.01 \text{ pc} \leq R_{\text{flat}} \leq 0.06 \text{ pc}$. For the setup used here, we employ $p = 2$ and $R_{\text{flat}} = 0.03 \text{ pc}$ (like in e.g. Seifried & Walch 2015) and we do not apply any cut-off radius or density. Hence, the radial density profile extends essentially to infinity.

The filament has a length of $L_{\text{fil}} = 2 \text{ pc}$, thus ranging from -1 to $+1 \text{ pc}$. In order to avoid a pressure jump at the outer edges of the filament we let the density decay exponentially for distances larger/smaller than $\pm 1 \text{ pc}$ along the major axis.

Following Ostriker (1964) there exists a critical filament mass per unit length above which the filament is unstable to perturbations and will undergo gravitational collapse. This critical *thermal line-mass* is given by

$$\left(\frac{M}{L}\right)_{\text{crit}} = \frac{2c_s^2}{G}, \quad (2)$$

where G is Newton's constant and c_s is the sound speed. The simulations are isothermal with $T = 15 \text{ K}$, which results in a critical line-mass of $(M/L)_{\text{crit,thermal}} = 24 M_{\odot} \text{ pc}^{-1}$. The central density ρ_{ridge} is varied to produce filaments with line-masses of $(M/L)_{\text{fil}} \sim 1.6 \times (M/L)_{\text{crit,thermal}}$ as well as of $(M/L)_{\text{fil}} \sim 0.8 \times (M/L)_{\text{crit}}$, where only gas within $R = 0.1 \text{ pc}$ is taken into account.

Observations have revealed that the interstellar medium and molecular clouds – and hence filaments – are turbulent and magnetized (see e.g. Elmegreen & Scalo 2004; Mac Low & Klessen 2004; McKee & Ostriker 2007; Crutcher et al. 2010; Crutcher 2012; Schmidt et al. 2013, and references therein). The turbulence is modelled by employing a turbulent velocity field, which is being generated in Fourier space with

$$E(k) \propto \begin{cases} k^{10} & k < k_{\text{int}} \\ k^{-2} & k > k_{\text{int}} \end{cases}, \quad (3)$$

where the slope at $k > k_{\text{int}}$ is typical for supersonic/shock-dominated turbulence and k_{int} being the integral scale. Using a box length of $L_{\text{box}} \sim 6 \text{ pc}$ in each spatial direction, the integral scale is $L_{\text{int}} \sim L_{\text{box}}/k_{\text{int}} \sim 1 \text{ pc} \sim 30 \times R_{\text{flat}}$. The turbulence is not driven and decays after approximately a crossing time.

Magnetic fields in molecular clouds have been shown to be approximately constant as a function of density up to a threshold density of $n_{\text{thresh}} \sim 300 \text{ cm}^{-3}$ (Crutcher et al. 2010; Crutcher 2012). For $n > n_{\text{thresh}}$, the magnetic field scales with density as $B \propto n^{\alpha}$ with $\alpha \sim 0.5\text{--}0.65$ (Crutcher 2012). However, the scatter in these Zeeman observations is rather large and we follow the approach by Seifried & Walch (2015) and set $B = 40 \mu\text{G} = \text{const}$. As these authors note, this value for the magnetic field strength is rather low but still in agreement with observational data. The simulations are initialized with two different orientations of the magnetic field, namely (a) \mathbf{B} being perpendicular to the filament's major axis and (b) \mathbf{B} being parallel to the filament's major axis. An overview of the initial conditions explored here is given in Table 1.

2.3 Chemistry

Deuterium fractionation is followed together with the hydrodynamical equations by employing the chemistry package KROME. We specifically emphasize that the network distinguishes between the ortho and para states of H_2 , H_3^+ , and H_2D^+ , where H_2D^+ is the main tracer of the deuteration fraction employed in the simulation (Walmsley et al. 2004). We assume the gas to be fully depleted, an assumption which becomes suitable above number densities of 10^4 cm^{-3} , given the very short freeze-out time-scale at our densities, and then applies to our initial conditions. The details and the uncertainties of the network have been largely discussed in Körtgen et al. (2017). We include the formation of molecules on the surface of grains but we do not take into account potential grain-surface processes as the H_2 ortho-to-para conversion on dust which can potentially accelerate the deuteration process (Bovino et al. 2017). The latter would introduce in fact additional free parameters into the calculation, and here our main interest is to establish a lower limit based on a standard network. The initial H_2 ortho-to-para ratio is 3 and the initial cosmic ray flux $\zeta = 1.3 \times 10^{-17} \text{ s}^{-1}$. We note that the cosmic ray flux together with the initial H_2 ortho-to-para ratio can strongly affect the deuteration process (see e.g. Kong et al. 2015). The uncertainties of these quantities are still very large and a quantitative study on the effect of these parameters on our simulations is beyond the scope of this study. However, in Section A we

²Webpage KROME: <http://www.kromepackage.org/>.

Table 1. Overview of the initial conditions for the performed simulations. All listed quantities are measured within a radius of $R=0.1$ pc. Columns 4 and 5 depict the critical line–mass, where in the latter the magnetic field and turbulence are taken into account. The Alfvén speed \mathcal{M}_a is calculated by using the average density within the radius R . The last two columns denote the free-fall times as calculated for a sphere or a cylinder (Toalá et al. 2012) with average density that is given in column 2.

Run name	ρ_{ridge} (g cm^{-3})	$\langle n \rangle$ (cm^{-3})	$(M/L)_{\text{crit,th}}$ ($M_{\odot} \text{ pc}^{-1}$)	$(M/L)_{\text{crit,tot}}$ ($M_{\odot} \text{ pc}^{-1}$)	B (μG)	Orientation	\mathcal{M}_{rms}	\mathcal{M}_a	$t_{\text{ff,sph}}$ (kyr)	$t_{\text{ff,cyl}}$ (kyr)
ML1.6-M0.6-Perp	4×10^{-19}	3.4×10^5	24	95.4	40	Perpendicular	0.6	0.38	57	92
ML1.6-M2.0-Perp	4×10^{-19}	3.4×10^5	24	175	40	Perpendicular	2.0	1.28	57	92
ML1.6-M2.0-Para	4×10^{-19}	3.4×10^5	24	175	40	Parallel	2.0	1.28	57	92
ML1.6-M4.0-Para	4×10^{-19}	3.4×10^5	24	467	40	Parallel	4.0	2.56	57	92
ML1.6-M6.0-Perp	4×10^{-19}	3.4×10^5	24	700	40	Perpendicular	6.0	3.84	57	92
ML0.8-M2.0-Perp	2×10^{-19}	1.7×10^5	24	233	40	Perpendicular	2.0	0.90	81	129
ML0.8-M6.0-Perp	2×10^{-19}	1.7×10^5	24	1050	40	Perpendicular	6.0	2.71	81	129

briefly discuss two control simulations with varying initial cosmic ray flux.

3 RESULTS

In the following, we will first discuss the global results for our reference run ML1.6-M4.0-Para, and subsequently assess the dependence of the deuterium fraction on the properties of the cores in different simulations. We then address the time evolution of typical cores as well as their radial profiles.

3.1 Reference run

To get an impression on the global dynamics, we first focus on our reference run ML1.6-M4.0-Para, with an average filament density of $3.4 \times 10^5 \text{ cm}^{-3}$. The line–mass corresponds to 1.6 times the thermal critical line–mass, or 0.09 times the critical line–mass when considering the magnetic field and turbulent fluctuations. The magnetic and turbulent pressure thus play a crucial role in stabilizing the filament against gravitational collapse. The magnetic field strength is $40 \mu\text{G}$, and the field is parallel to the filament major axis. The free-fall time of the system, considering the cylindrical geometry ($t_{\text{ff,cyl}} = \sqrt{R_{\text{fil}}/2L_{\text{fil}}G(\rho)}$, Toalá et al. 2012), corresponds to 92 kyr. The system of course is not going through free-fall due to the stabilizing effect of the magnetic field and turbulence, but it provides a characteristic time-scale for larger scale motions within the filament. In Fig. 1 we show snapshots of the column density and the density-weighted deuterium fraction

$$D_{\text{frac}} = \frac{\int \frac{[\text{H}_2\text{D}^+]}{[\text{H}_3^+]}\rho dz}{\int \rho dz}, \quad (4)$$

in the x – y plane, that is, perpendicular to the initial magnetic field. In equation (4) ρ is the density in each cell, dz denotes the path-element (essentially the cell size) along the z -direction and $[X]$ denotes the mass fraction of species X in that cell. The different maps correspond to 0.5, 1, 2, and 2.2 times the free-fall time (from top to bottom). At early times, $t \sim 0.5 t_{\text{ff,cyl}}$, the innermost part near the ridge of the filament has already accreted mass and thereby enhanced column density. This increase is, however, not uniform along the major axis, but rather scattered throughout the filament due to compression and dilatation of individual gas parcels by turbulent motions. At the same time, the filament is observed to be slightly bent on larger scales due to the ambient turbulence in the filament itself as well as in the more diffuse gas surrounding it. At about one free-fall time ($t \sim 90$ kyr), individual overdense regions can readily be identified. At the same time, the filament breaks up at $x \sim 0.6$ pc and

$x \sim 1.3$ pc, a feature that can be associated with dispersion due to turbulence and material flowing along the magnetic field lines towards deeper gravitational potential wells. Interestingly, striations appear in the diffuse gas, which are more pronounced near overdense regions within the filament. Such striations are frequently seen in observations in the context of a hub-filament with ‘sub’-filaments surrounding it (e.g. Myers 2009). These features are generated, in this reference run, via gravitational focusing due to the overdense structures within the filament.

The further evolution of the filament reveals stronger bending of the whole structure as well as ongoing fragmentation within the filament. The amplitude of the bending is ~ 0.1 – 0.2 pc. The fragments show signs of ongoing accretion (observed by their increased column density), but some also seem to dissolve. The striations in the surroundings of the filament have now also become denser and, at least for the structure at $x \sim -0.5$ pc, they appear to be tightly connected to the inner part of the filament. From 180 kyr to the end of the simulation at 200 kyr, the filaments do not evolve very much, but differences are seen for some of the overdensities. At the same time, the previously mentioned breakup of the filament proceeds, revealing regions with a decrease in column density by about an order of magnitude.

On the right side of Fig. 1 the deuterium fraction is shown for the same temporal stages as discussed above for the column density. In general it is observed that this ratio traces the density quite well. This is to be expected, as chemical time-scales depend on the density, and also the deuterium fractionation process is faster at higher densities. Initially the deuterium ratio is rather small of the order of $\lesssim 10^{-3}$ throughout the whole region. When the filament is evolving in time, the process of deuterium fractionation becomes less efficient in the outskirts due to the reduced density compared to the inner part. At around one free-fall time the deuterium fraction is readily enhanced in the innermost part of the filament, again matching quite well the overall density structure. In addition, the deuterium fraction appears to be almost homogeneous throughout the filament. However, individual overdensities can be identified. At late times, deuterium fractionation becomes also efficient in the more tenuous gas surrounding the filament. The inner ridge of the filament has now significantly increased deuterium fractions of the order of 0.01–0.3. In this sense, regions of strongly increased density show the highest values, as is expected. Interestingly, the previously mentioned striations also show an enhanced deuterium fractionation, giving rise to accretion of highly deuterated gas on to regions within the filament. If one compares the filament at $t = 180$ kyr and $t = 200$ kyr, interesting features appear. Although the time evolution of the overall column density between these stages is

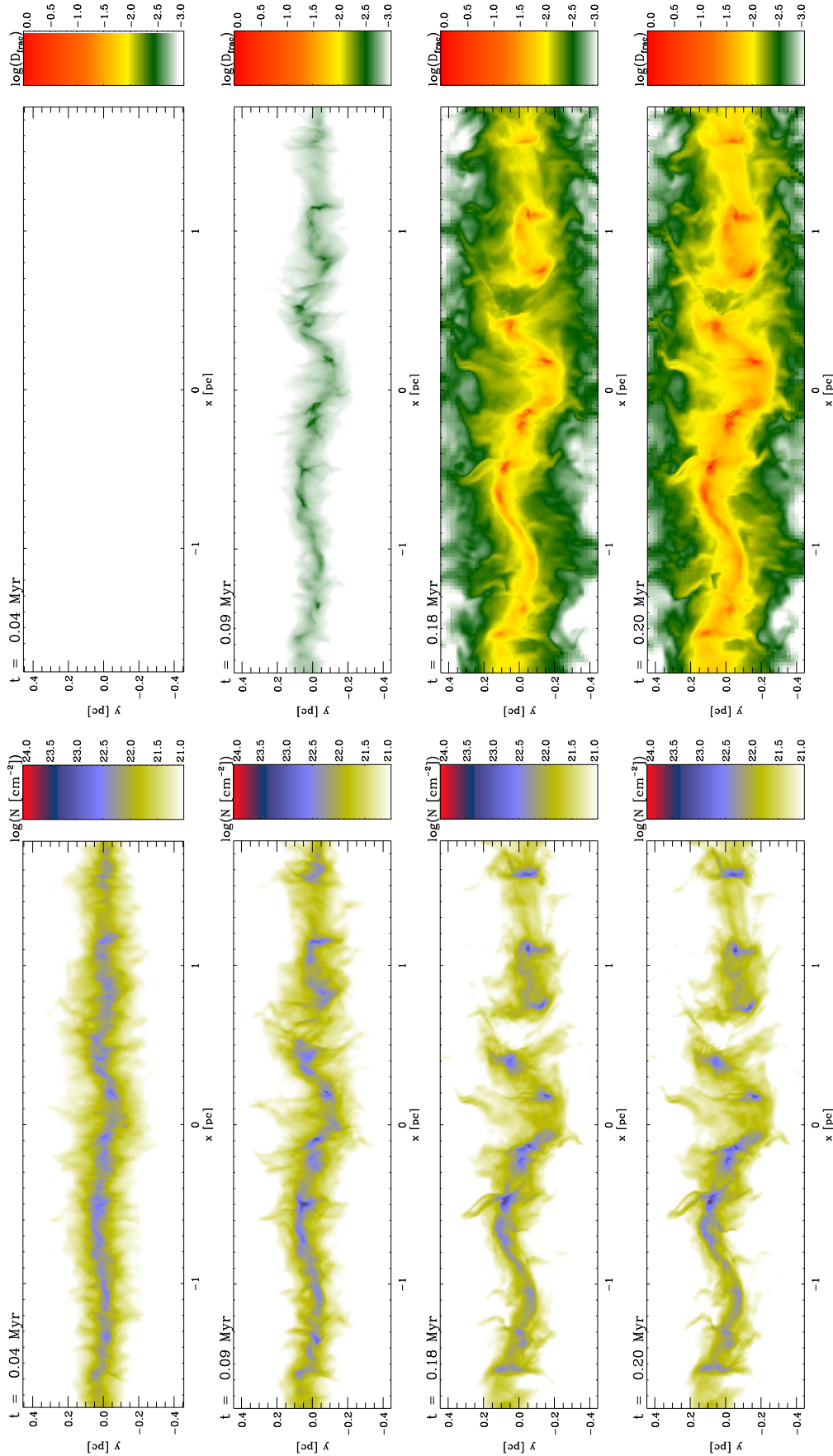


Figure 1. Time evolution of the filament in run ML1.6-M4.0-Para. *Left:* Top-down view of column density for density-weighted deuterium fraction. The initially strong turbulence leads to a heavily bent and partially disrupted filament. Individual cores form due to compression. The times shown refer to 0.5, 1, 2, and 2.2 free-fall times. The integration length is $l = 0.2$ pc.

rather small, the deuteration fraction evolves significantly. In detail, the gaps that formed due to mainly turbulent fluctuations appear to be smoother when looking at the deuteration fraction at these times. Although the column density is greatly reduced in these gaps, the density is still high enough to promote a rather efficient deuteration process.

3.2 Dependence of the deuterium fractionation on core properties

Of particular interest in our investigation is how the properties of the cores evolve over time, and if there are statistical correlations between different properties of the core. We are particularly interested in potential correlations of the deuteration fraction with core mass, H_2 density, and the virial parameter, which are plotted in Fig. 2 at 0.5, 1, and 2 free-fall times as defined for cylindrical systems. As shown in Table 1, the value of the filament free-fall time varies between 92 and 129 kyr for our simulations. The individual cores are defined as spatially connected (i.e. neighbouring cells with similar density) structures with a lower threshold density of $n_{\text{min}} = 8 \times 10^4 \text{ cm}^{-3}$. However, we caution here that the term *core* is somewhat ill-defined and mostly based on whether the object can be distinguished from the background.

For all three quantities, we find an initially flat relation at 0.5 free-fall times. This corresponds to the stage where the cores have initially formed, and where their chemical properties are thus dictated by the average evolution within the filament. Therefore, we see no dependence on the parameters of the core. We note that, at this temporal stage, the chemistry already evolved for $\sim 40\text{--}50$ kyr together with the hydrodynamics, thus setting the properties of the cores in a self-consistent way. This is different at one free-fall time, where a mild increase of deuteration fraction is visible as a function of both core mass and H_2 number density. The correlation with H_2 density is expected from a chemical point of view, as it enhances the deuteration rate, and it appears that (with some scatter) the density is correlated with the core mass. In this context, it is consistent that the correlation appears more pronounced when looking at D_{frac} versus density. After two free-fall times, these trends become even more clear and are particularly well visible in our reference run, which includes a larger number of cores. We however also see that there is a dependence on the initial conditions of the filament, as for instance the simulation ML0.8-M2.0-Perp has two cores that follow the same trend, but with enhanced values of D_{frac} compared to the reference run, while ML1.6-M0.6-Perp shows lower values. While it seems plausible that we can expect typical correlations, their normalization may vary from filament to filament.

In the plots of D_{frac} as a function of the virial parameter, we find the inverse correlation, i.e. decreasing deuteration fractions for increasing virial parameters. We note that many of the cores that are defined via density thresholds have virial parameters larger than 1, and are thus not gravitationally bound. This may at first seem surprising, but also observed samples of cores show high virial parameters of order 20 (Kauffmann et al. 2013; Kirk et al. 2017, and references therein). The inverse correlation is then not surprising, as a core with higher virial parameter will typically have lower density, which reduces the efficiency of chemical reactions including deuterated species. These cores might also have higher velocity dispersions, which tend to dissolve these regions, thereby reducing the density and hence again the efficiency of chemical reactions. This trend is still weak at about one free-fall time, but pronounced at two free-fall times.

3.3 Time evolution of core properties

To illustrate how the cores in our simulations evolve over time, we now focus on a set of randomly selected cores that are summarized in Table 2.

We only consider cores from filaments that have been evolved for at least 190 kyr in order to have a suitable amount of time evolution, which covers the initial as well as the more evolved stages of the filament.

In Fig. 3, we show the average number density and mass of the cores as a function of time. Most of them do significantly increase as a function of time, with initial number densities of 10^5 cm^{-3} and later values of up to 10^7 cm^{-3} , and masses from initially $0.01\text{--}0.1 M_{\odot}$ up to later $10\text{--}100 M_{\odot}$, during an evolutionary time of about 200 kyr. Both quantities show significant scatter, arising from the somewhat arbitrary definition of the cores and the density fluctuations that will naturally occur during the evolution. The latter point indeed emphasizes that the cores within the filaments are highly dynamic and not static objects. We also see that in one case, corresponding to ML0.8-M2.0-Perp, both number density and mass of the clump are not increasing. The latter thus corresponds to an object that is strongly stabilized by magnetic fields (the core's Alfvén Mach number is ~ 0.2 throughout its evolution), and will potentially never lead to star formation.

To better understand the subsequent further evolution of the cores, we now turn to Fig. 4, showing the virial parameter and the mass-to-flux ratio as a function of time. These quantities vary again strongly between the cores, in terms of both their initial values and their evolution. In two cases, for ML0.8-M2.0-Perp and ML1.6-M4.0-Para, the virial parameter never drops below 1, suggesting that they may never go through gravitational collapse. The second case is partly reflected in Fig. 3, where the density increases over 200 kyr corresponded to a factor of 3–4, implying at best a very slow collapse. Interestingly, we nevertheless see no difference in the deuteration fraction for this case. For the other cases the virial ratio drops close to or below a value of 1 during their evolution, and are thus gravitationally unstable. However, also for these cores, the scatter in the time evolution of the dynamical parameters is rather large.

A similar behaviour can be seen in the mass-to-flux ratio within the same figure, where all cores start out with mass-to-flux ratios of $0.01\text{--}0.1$. Consistent with the results above, ML0.8-M2.0-Perp remains at this low value, while ML1.6-M4.0-Para at least comes close to a value of 1 (and crosses the value temporarily). All other cores show a growing mass-to-flux ratio with time, explained by their rapid collapse as visible through the density evolution. We therefore conclude that the initial mass-to-flux ratio of a clump does not necessarily reflect this ratio at later stages of the evolution.

We now explore the chemical properties in Fig. 5, showing the mass-weighted deuteration fraction and H_2 ortho-to-para ratio as a function of time. We find a similar evolution in almost all cases, with slight differences only in the case of ML0.8-M2.0-Perp, where the evolution of mass and density is considerably different from the other cores. The other cores (and even still this one) show a remarkable similarity in their chemical evolution, with the H_2 ortho-to-para ratio steadily decreasing as a function of time, with an initial value of ~ 0.3 at core formation, down to a value of 0.001 after about 250 kyr of evolution. These values are in agreement with the ones assessed via observations. For instance, an ortho-to-para ratio of 0.1 was found in the pre-stellar core L183 (Pagani et al. 2009), and 10^{-4} towards IRAS 16293–2422 (Brünken et al. 2014).

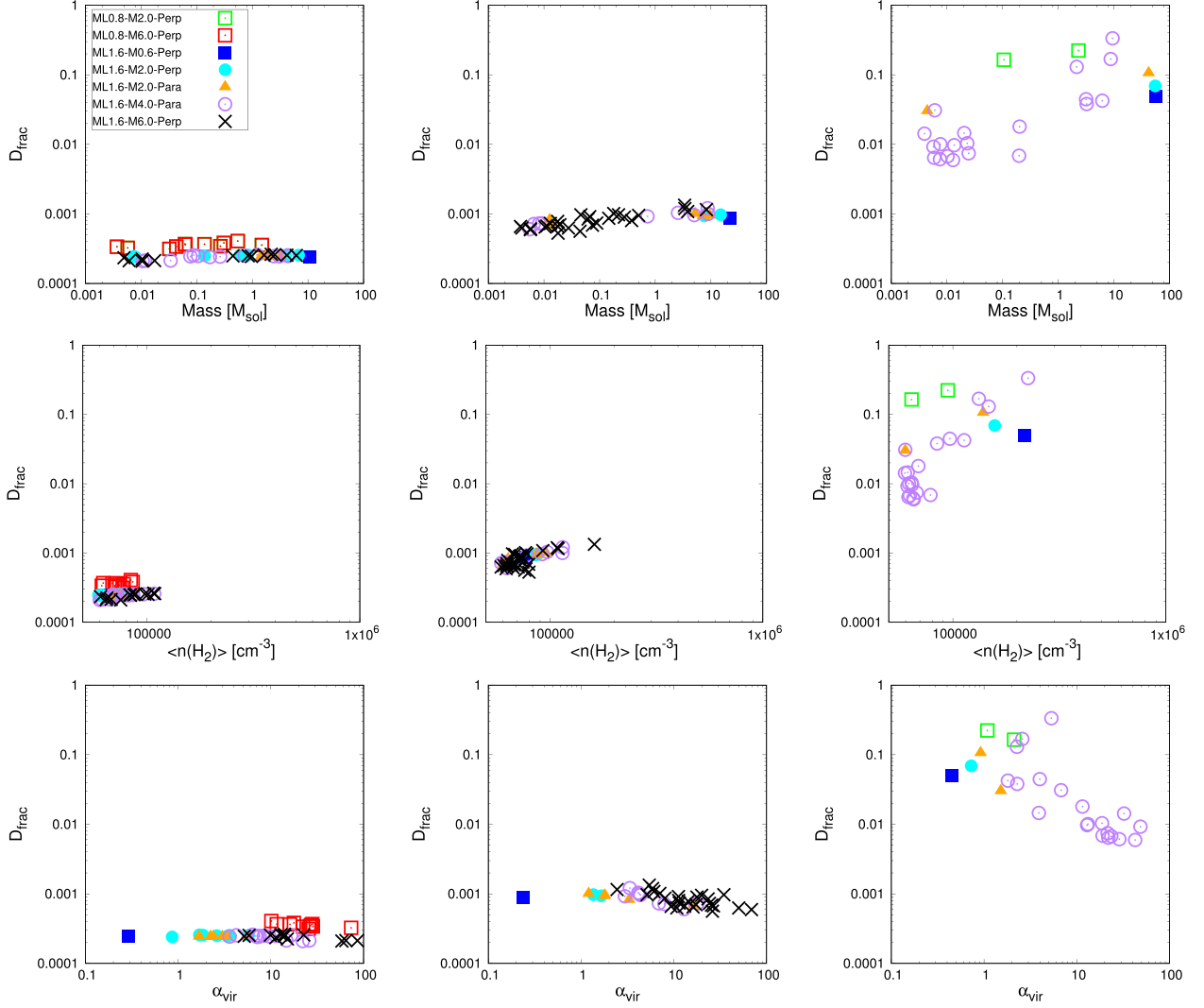


Figure 2. Statistical properties of the cores found in the different simulations. We plot the deuteration fraction as a function of core mass (top panel), average H_2 density (mid panel), and virial parameter (bottom panel) at three characteristic times in the simulations, corresponding to 0.5, 1, and 2 free-fall times as defined for cylindrical systems. For times $t < t_{\text{ff,cyl}}$, the chemical evolution is dominated by the average density of the filament and appears to be independent of the dynamical properties of the filament. At late stages, trends emerge, which can be assigned directly to the properties of the cores, but indirectly also to their formation time. In this respect, low- D_{frac} cores shown at later stages should have formed later. This is also in agreement with Fig. 1, where the major part of the filament shows $D_{\text{frac}} \sim 0.01$.

Table 2. Overview of time-scales and density of selected cores for the different filaments. The second column denotes the time when the core is being identified for the first time. The third and fourth columns give average core density and free-fall time at first identification point. The following two columns denote the end of the simulation and the evolution of the core in number of free-fall times (calculated using average density from column 3). The last two columns state the maximum average deuterium fractionation in the cores and the number of free-fall times to reach this value.

Run name	Identification time (kyr)	Average density (cm^{-3})	Free-fall time (kyr)	Ending time (kyr)	Number of free-fall times	Maximum mean D_{frac}	Free-fall times to $D_{\text{frac,max}}$
ML0.8-M2.0-Perp	65.4	7.8×10^3	376.66	351	0.76	0.068	0.68
ML1.6-M0.6-Perp	130	2.7×10^5	63.90	253	1.92	0.054	1.92
ML1.6-M2.0-Perp	55.5	1.0×10^5	103.50	193	1.33	0.019	1.33
ML1.6-M2.0-Para	68.7	1.5×10^5	86.50	257	2.18	0.099	2.16
ML1.6-M4.0-Para	49.1	6.2×10^4	133.72	202	1.14	0.027	1.14

The decrease of the ortho-to-para ratio of H_2 over time in turn also boosts the deuterium fractionation, where this ratio starts at a value of ~ 0.001 at core formation, and reaches values of ~ 0.1 after about

250 kyr. A similar value is even reached in the non-collapsing core ML0.8-M2.0-Perp, even though on a somewhat longer time-scale of 300–350 kyr. This is in fact in agreement with the observational

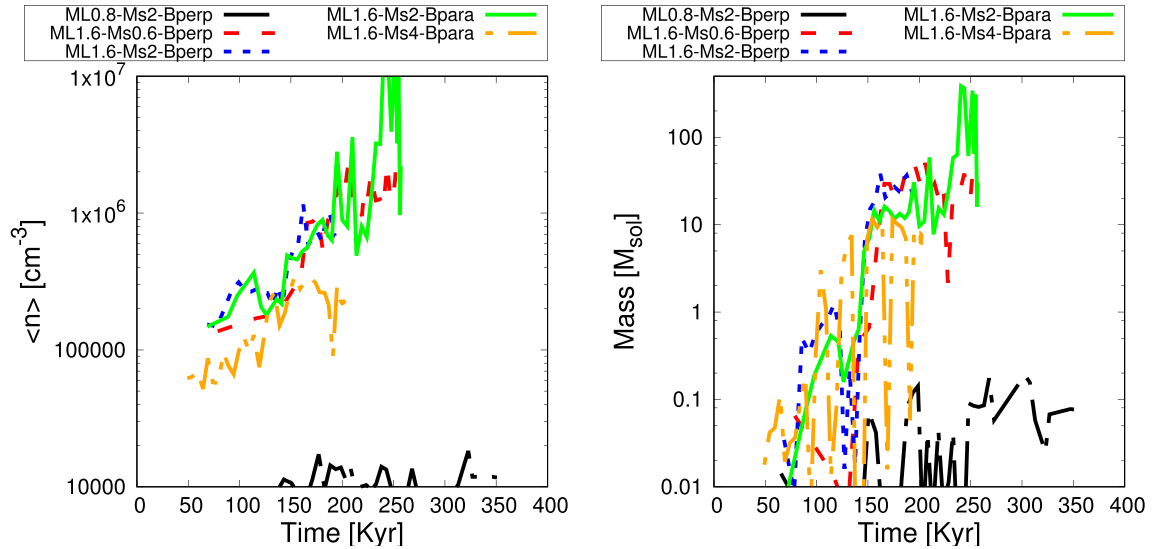


Figure 3. *Left:* Evolution of average volume number density of the cores given in Table 2. When the filament is initially sub-critical the core density is roughly 10^4 cm^{-3} and hence on the verge of applicability of our model. *Right:* Time evolution of core mass. It is evident that the current setup of filaments provides a large enough mass reservoir that the core can become massive in a rather short time, but we emphasize that we only follow the evolution *before* star formation. The scatter in the evolution comes from the highly dynamic environments of the cores, but also due to our somewhat arbitrary definition of a core.

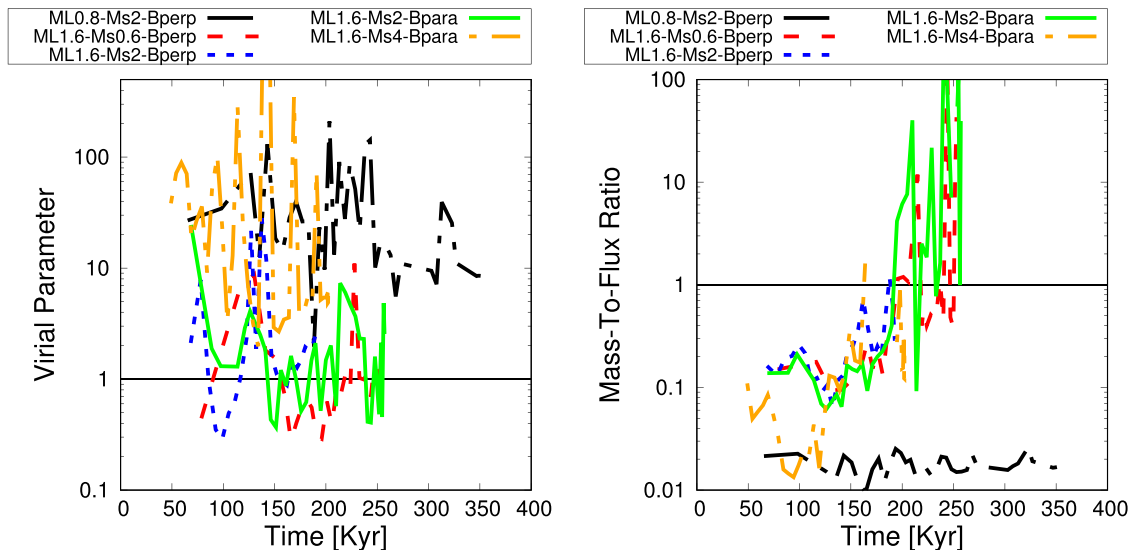


Figure 4. Evolution of virial parameter (left, only turbulent velocity taken into account) and mass-to-magnetic flux ratio (right) as function of time for the cores given in Table 2.

findings by Fontani et al. (2011), who give an evolutionary sequence for the deuterium enrichment in pre-stellar cores and ultracompact HII regions. In addition, the deuteration fraction in the core of run ML0.8-M2.0-Perp starts to saturate, which is due to the fact that the density in the core does not evolve at all.

In Fig. 6 we show column density maps of selected cores in the thermally supercritical filaments at the end of the individual simulation. The filament with initially subsonic turbulence (first row) reveals a highly ordered morphology since this filament collapsed almost unimpeded along the radial direction. The ambient turbulent fluctuations in the gas still lead to the formation of individual small-scale overdensities with a rather regular spacing. If seen edge-on, these structures seem to accrete material from the diffuse environment, thereby generating fingers of increased column density. The

selected core can be clearly identified in the rightmost picture as the structure with spiral-features.

In contrast, if the initial turbulent fluctuations are supersonic (rows 2–4), the filaments become locally highly disordered as can be seen from the other figures. The selected cores now appear to be in isolation as overdense structures surrounded by a high-density halo. However, this halo is not spherical and its morphology is linked to the orientation of the ambient magnetic field as can be seen by the morphological difference between the cores with parallel or perpendicular magnetic field. We emphasize that in all cases the cores resemble oblate rather than spherical objects due to significant angular momentum in this region.

All cores reveal an order of magnitude or larger increase in column density with respect to their ambient medium. However, the

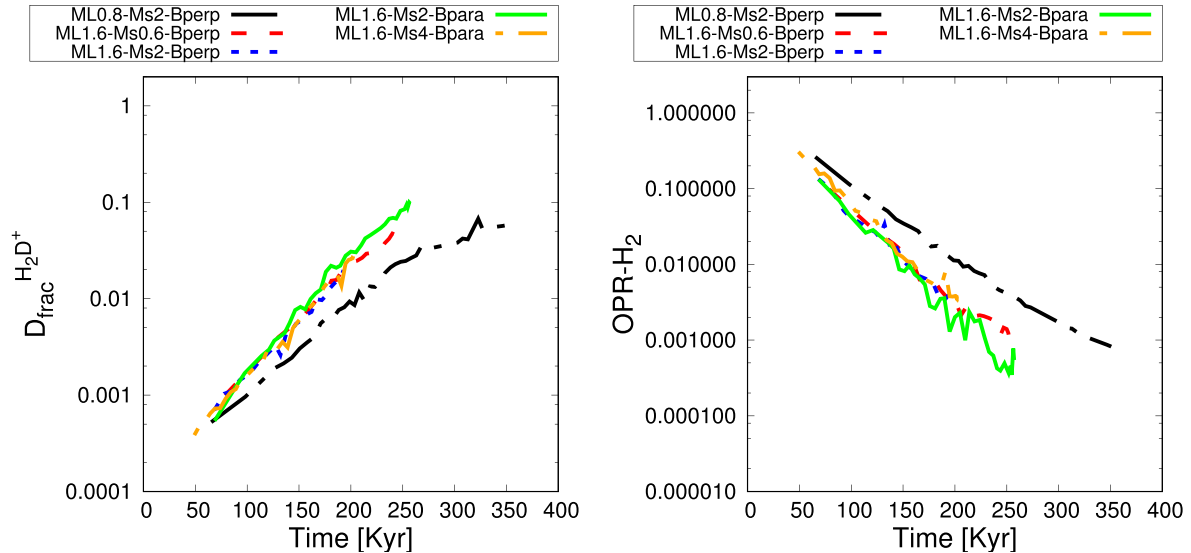


Figure 5. Time evolution of average deuteration fraction (left) and OPR- H_2 (right) in the cores given in Table 2. Averaging is performed only within a single core. Although the initial OPR- H_2 is set to the conservative value of 3, the actual OPR at core formation is about an order of magnitude lower already after only 50 kyr ($\sim 0.5 t_{\text{ff,cyl}}$) of evolution.

virial parameter and mass-to-flux ratio, as shown in Fig. 5, indicates that these objects are still not gravitationally unstable, but are in an equilibrium configuration, where any significant increase in density/mass will drive them unstable.

The deuteration fraction of the selected cores and their environment is shown in Fig. 7. Similar to the column density maps, the filament in run ML1.6-Ms0.6-Bperp reveals a thin region of greatly enhanced deuteration fraction with values of $D_{\text{frac}} \sim 0.5\text{--}0.9$. Interestingly, the deuteration appears to be widespread and enhanced also in the more diffuse gas surrounding this filament, as can be seen from the middle panel. However, a closer look to the left-hand panel shows that the area of enhanced deuteration fraction only extends along the z -direction. The magnetic field in this filament is initially oriented along the y -direction (i.e. perpendicular to the major axis) and hence this increase can be associated with overdensities formed by converging motions along the field lines towards the inner part with a deeper gravitational potential well. The only other filament with enhanced deuterium fractionation in the environment is the one with initial Mach number of $\mathcal{M} = 2$ and a parallel oriented magnetic field (see also Pillai et al. 2012, for observational evidence of widespread deuteration). In this scenario, the field provides support against radial contraction, thus giving the gas enough time to build up a sufficiently large amount of H_2D^+ compared to H_3^+ . In addition, turbulent mixing also leads to high deuterium fractionation in the more diffuse gas. The other two filaments ML1.6-M2.0-Perp and ML1.6-M4.0-Para only show a small region of enhanced deuteration fraction, while the outskirts reveal values of $D_{\text{frac}} \sim 0.01$. A closer look at the latter filament highlights that the material surrounding the core has a slightly higher value of D_{frac} due to the stabilizing effect of the (parallel) magnetic field and the larger amount of turbulence. Overall, our results thus demonstrate that deuteration in the denser gas is highly efficient and largely independent of the specific evolution within the cores.

3.4 Radial profiles of selected cores

We finally analyse the radial profiles of the selected cores at different times, focusing on deuteration fraction, surface density as well as

H_2 ortho-to-para ratio. The corresponding plots are given in Fig. 8 for the different cores. We use the centre of mass to define the core centre, which leads to surface density peaks not associated with the centre of the profile.

In our special case ML0.8-M2.0-Perp, which is stable against collapse, the surface density is hardly evolving and remains at low values with $0.1\text{--}1 \text{ g cm}^{-2}$. This is different in all other runs, where the surface density is significantly increasing and reaching values of $10\text{--}100 \text{ g cm}^{-2}$ within 200 kyr. The runs with magnetic fields parallel to the filament show a particularly prominent peak of the surface density at $1000\text{--}2000 \text{ au}$, and a somewhat milder peak in ML1.6-M2.0-Perp with perpendicular field structure. Overall, many of the surface density structures appear consistent with the results found for collapsing cores by Körtgen et al. (2017), suggesting that the characteristic peak is moving outward with increasing turbulent Mach number. Again similar to the Körtgen et al. (2017) results, the H_2 ortho-to-para ratio has only a weak dependence on the underlying density structure, and appears as approximately flat within the radial profile, with small dips in the places of the surface density peak, as the ratio decreases more efficiently at high densities. Apart from such specific features, the results for the ortho-to-para H_2 appear quite comparable between the different cores.

The deuteration fraction is again reflecting the density structure more strongly, with pronounced peaks in the runs with parallel fields, and somewhat weaker / reduced peaks in runs with perpendicular field structures. The latter may be indicative of a different mode of fragmentation and core formation, as also suggested by Seifried & Walch (2015), and therefore explain the differences in the structure. Even given these differences, quite high deuteration fractions up to values ~ 1 are reached in almost all cases through a rather monotonic evolution. The only partial exception is ML0.8-M2.0-Perp, the non-collapsing core, where the deuteration fraction even slightly decreases between 250 and 350 kyr, and never exceeds values of 0.05. We attribute this to the overall particular evolution in this case, where also the surface density decreases over time, suggesting a strong interaction and exchange between the core and its environment. However, it is important to say that values of about $10^{-3}\text{--}10^{-2}$ already represent enhanced deuteration and have been

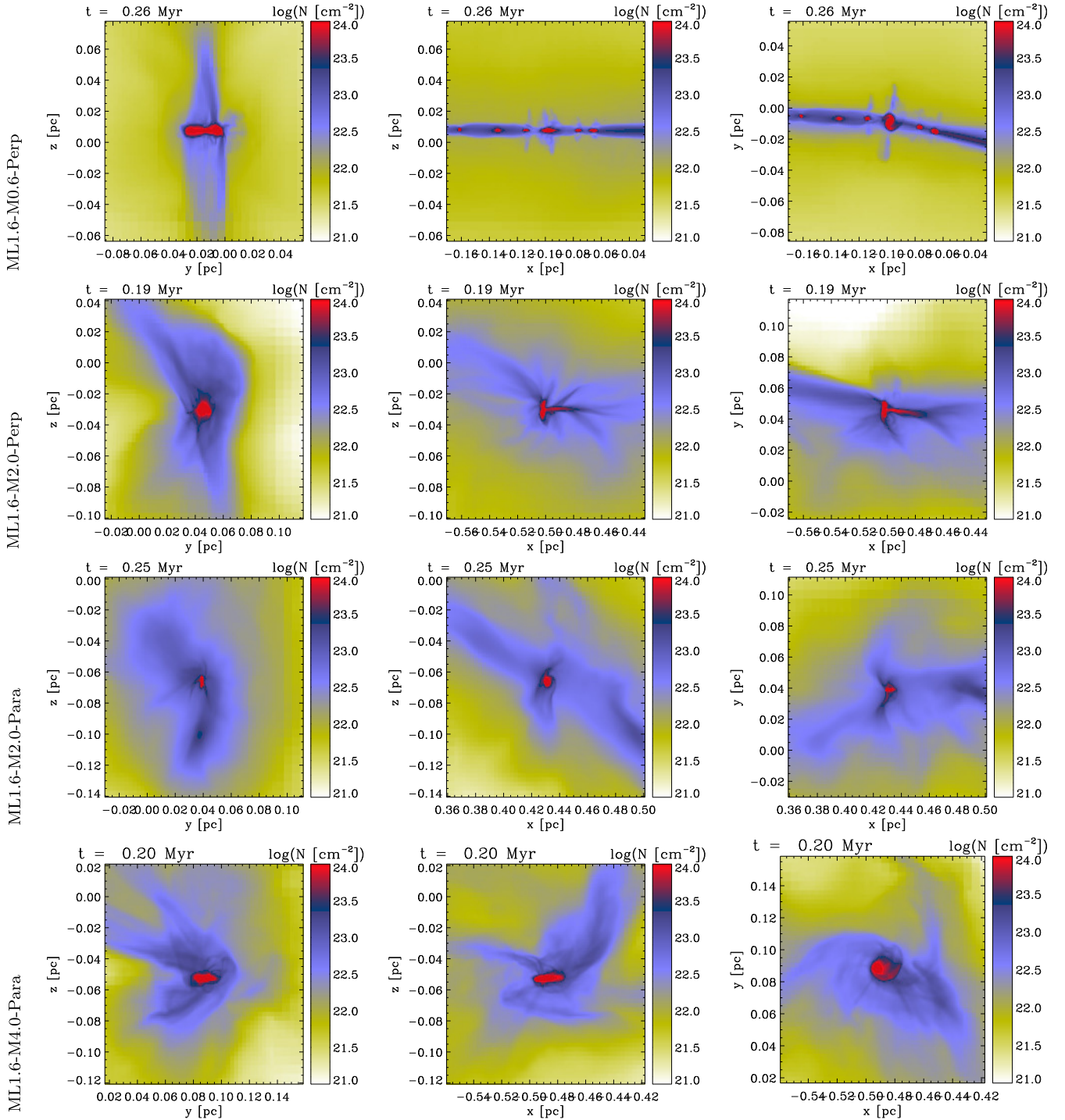


Figure 6. Zoom-in to selected cores in different filaments at the end of the simulation. Shown is the column density along different directions. Integration length in all cases is $l = 0.2$ pc. All cores reveal an oblate geometry. Only with initially supersonic turbulence, the core environment becomes highly irregular and dynamic. Note the finger-like structures of enhanced column density near the cores.

reported in different observational works (e.g. Barnes et al. 2016; Lackington et al. 2016).

4 COMPARISON TO PREVIOUS STUDIES

Studying deuterium fractionation within the scope of 3D models is a relatively new approach. Previous studies focused on 0D or 1D approaches to explore the process of deuterium fractiona-

tion (e.g. Flower et al. 2006; Kong et al. 2015; Sipilä & Caselli 2018). Thus, we here aim to briefly compare our findings to such works.

We find values of the *average* deuterium fraction between 0.01 and 0.1 within a time period of $t \lesssim 400$ kyr, which indicates that deuterium fractionation is rather efficient. By comparing this time evolution to the one in the work by Kong et al. (2015, i.e.

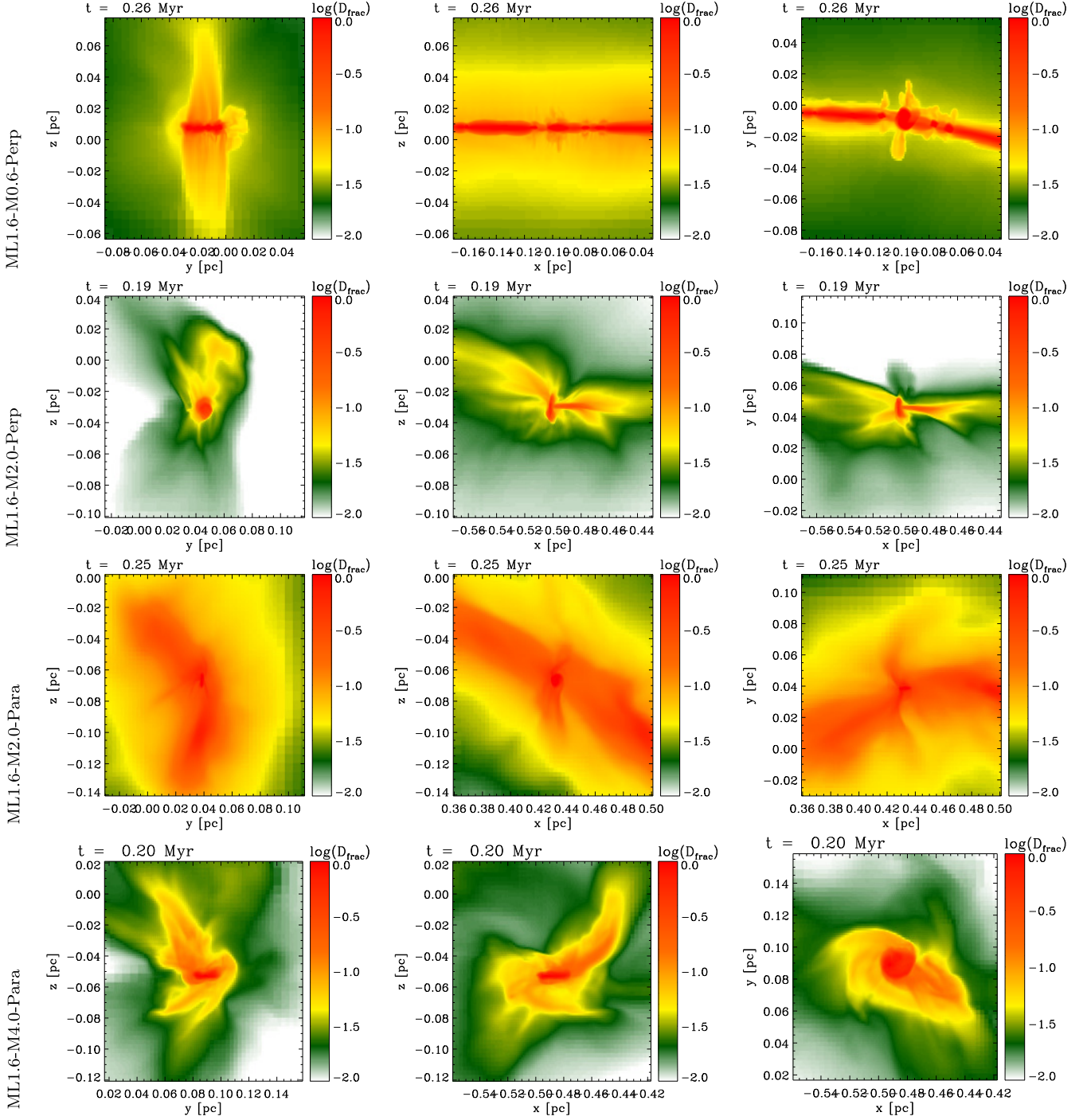


Figure 7. Deuterium fractionation of selected cores in different filaments at the end of the simulation. Shown is the deuterium fraction along different directions. Integration length in all cases is $l = 0.2$ pc. The previously mentioned high-density channels are also regions of greatly enhanced deuterium fraction, giving rise to accretion of highly deuterated material.

their fig. 5), we find a significantly enhanced deuterium fraction at such times. As these authors show, variations in the temperature only yield small changes of the point where the deuterium fraction starts to increase. Varying the density shows a stronger impact. For example, they find that the deuterium fraction starts to increase around $t = 200\text{--}500$ kyr after the start of the simulation at fixed densities of $n = 10^7 \text{ cm}^{-3}$. The values reached are a little smaller, but still comparable to the findings of this study. Since our cosmic

ray flux does not differ too much from their fiducial case, one is appealed to reject this as the major cause of the differences. However, Kong et al. (2015) also study the impact of the heavy-element depletion factor on the time evolution of the deuterium fraction. Their results indicate that an increase of the depletion factor from 10 to 1000 results in a decrease of the time needed to reach a certain value of the deuterium fraction by an order of magnitude, namely going from $t \sim 10^6$ yr to $t \sim 10^5$ yr to reach values of $D_{\text{frac}} \sim 0.1$.

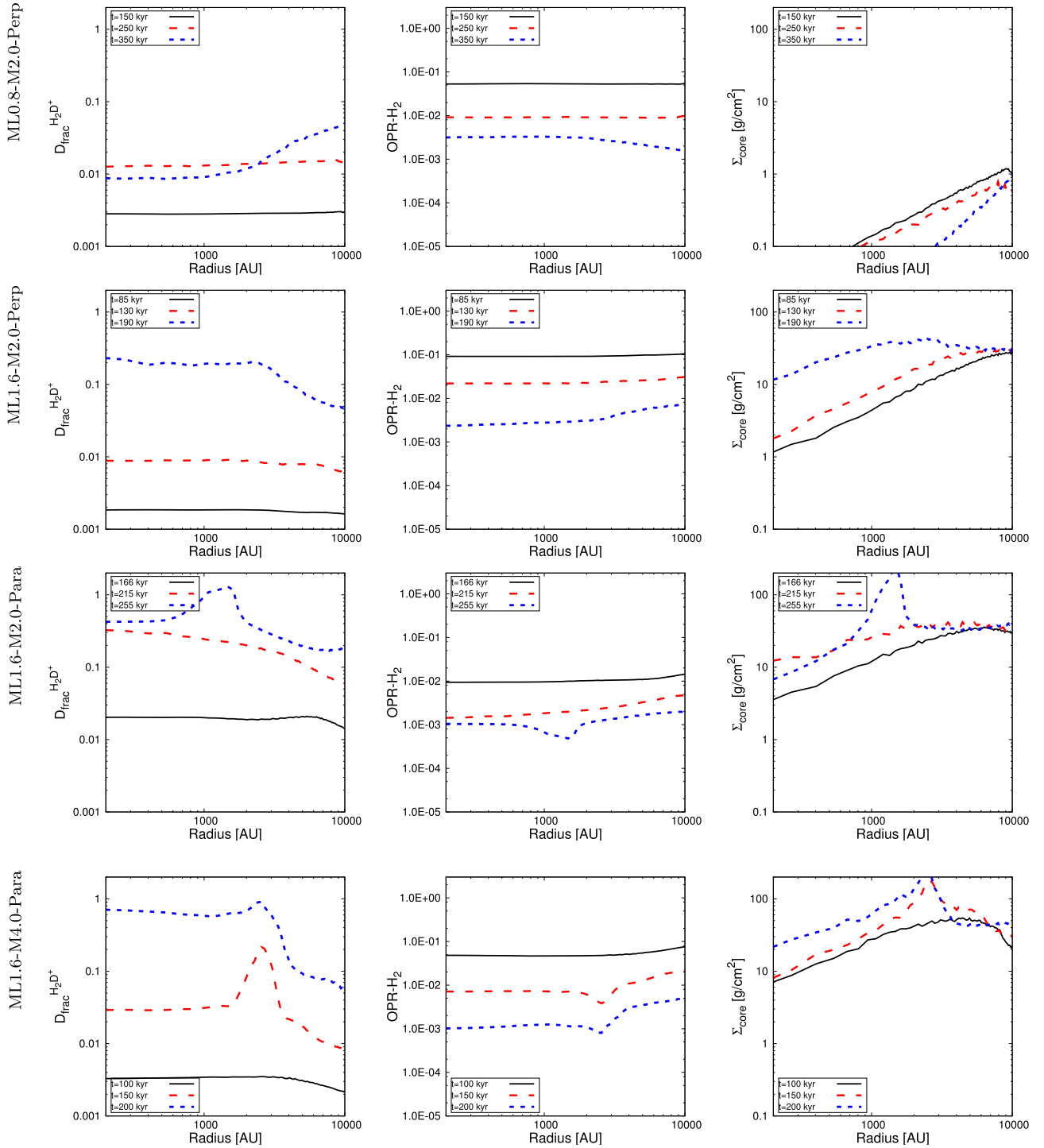


Figure 8. Radial profiles of deuteration fraction, H_2 ortho-to-para ratio, and gas surface density for the some of the selected cores at different times. It is observed that the deuteration fraction mainly follows the surface density, as is expected. The OPR- H_2 shows almost no variation along the profile, except some scatter collocated with peaks in the surface density. Note, the core centre is defined as the centre of mass and not as the point of maximum surface density.

These values for D_{frac} and the time-scales are in good agreement with our findings, given our strong assumption of complete heavy element depletion and the highly dynamical density evolution in the dense cores within the filament.

More recently, Sipilä & Caselli (2018) studied the chemical evolution in 1D models of either static or collapsing Bonnor–Ebert spheres. They find that, given the results at different times from

their fig. 5, H_2D^+ declines as function of distance from the core centre, whereas H_3^+ stays almost constant in the inner part of the core and declines at larger distances. From their results it is possible to infer a trend for the ratio of H_2D^+ over H_3^+ , which shows that the ratio declines with increasing distance. For smaller distances to the core centre, the decline is primarily due to a decrease in H_2D^+ . In general, this result is in agreement with the radial profiles of

selected cores from our 3D simulations (see Fig. 8), although we emphasize the different time evolution. Their simulated ortho-to-para ratio of H_2 (their fig. 5) is observed to be roughly constant in the innermost part of the core (distances $\lesssim 6000$ au), but increases sharply at larger distances. We can confirm that the ortho-to-para ratio is constant in the innermost part of the cores and that it starts to increase at larger distances. Furthermore, the spatial variation of the ortho- and para-species of H_2 depends on which core one refers to. However, for most of the cores in our Fig. 8, we find a similar behaviour of the ortho-to-para ratio of H_2 as a function of distance to the core centre.

In this sense, the results from our 3D framework are in agreement with previous lower dimensional studies. However, further 3D studies are needed to understand how sub-structures form and evolve over time and how these are affected by turbulence and magnetic fields.

5 SUMMARY

We have pursued here the first 3D magnetohydrodynamical simulations of filaments including a detailed chemical model to explore deuterium fractionation. For this purpose, we have adopted the network by Walmsley et al. (2004), assuming full depletion, valid in the inner 0.2 pc of our filaments, which is the main region we are interested in. We studied both the chemical evolution of the filament as a whole, as well as the formation and chemical evolution of individual cores. When investigating deuteration fraction as a function of core mass and density, we find an initially flat relation right after the formation of the cores, which increasingly steepens at more advanced evolutionary stages. The slope of this relation is thus potentially indicative of the evolutionary stage of the filament, even though we note that the normalization of the relation may vary from filament to filament depending on the initial conditions.

We subsequently considered the time evolution of a number of selected cores (based on the requirement that we have sufficient data to follow at least 200 kyr of evolution), finding a remarkably similar chemical evolution in all cores, including one that is strongly stabilized by turbulence and magnetic field and therefore not going through gravitational collapse. Assuming a more or less chemically homogeneous initial condition, the chemical evolution of the cores, particularly regarding deuteration effects, is thus very similar. Of course, environmental effects such as the local cosmic ray ionization rate could induce potential differences, by changing the ionization degree. Similarly, metallicity effects at lower densities may depend on the local conditions. At least within one filament, it is however plausible that the deuteration fraction is indeed indicative of chemical age. We find here that about two free-fall times (as defined for cylindrical systems, see Toalá et al. 2012) are sufficient to reach core deuteration fractions of $\gtrsim 0.1$. We finally investigated also the radial structure of the core, finding overall similar properties as in the isolated collapsing cores studied by Körtgen et al. (2017). The H_2 ortho-to-para ratio appears to be approximately flat and only weakly dependent on radius. Both the deuteration fraction and the gas surface density show a peak on scales of about 1000–2000 au, which is particularly pronounced in the case of parallel magnetic fields. As found previously, this peak moves outward with increasing turbulent Mach number, indicating the amount of support against gravity. The difference in the visibility of the peak may result from the difference in the fragmentation mode in both cases, as previously described by Seifried & Walch (2015), thus potentially affecting the structure of the resulting cores. Overall, our results have shown that the observed high deuteration fraction in prestellar

cores can be readily reproduced in simulations of turbulent magnetized filaments. We further found that deuteration fractions of order 0.1 can be produced independent of the specific history of the cores, both for high and low virial parameters. The latter suggests that deuteration is potentially very efficient.

While the main purpose of this study was to explore this feasibility in general terms, it is crucial that future investigations assess these results in further detail, by e.g. using improved chemical networks (Vastel et al. 2012; Majumdar et al. 2017). In addition, considering grain-surface effects may further enhance deuteration as for instance the ortho-to-para conversion process (Bovino et al. 2017). But also include a dependence on additional free parameters like CO freeze-out and cosmic ray flux would improve our knowledge on the entire process. We believe that such calculations will become feasible in the near future, and thus help to address the important question regarding the time-scale to achieve high deuteration fractions.

ACKNOWLEDGEMENTS

BK, SB, DRGS, and RB thank for funding through the DFG priority program ‘The Physics of the Interstellar Medium’ (projects BO 4113/1-2, SCHL 1964/1-2, and BA 3706/3-2). Furthermore RB acknowledges additional funding from the DFG for this project via the grants BA 3706/4-1 and BA 3706/15-1. DRGS thanks for funding through Fondecyt regular (project code 1161247), the ‘Concurso Proyectos Internacionales de Investigación, Convocatoria 2015’ (project code PII20150171), ALMA Conicyt (project 311600001), and the BASAL Centro de Astrofísica y Tecnologías Afines (CATA) PFB-06/2007. The software used in this work was developed in part by the DOE NNSA ASC- and DOE Office of Science ASCR-supported Flash Center for Computational Science at the University of Chicago. The simulations were performed on the local GPU cluster *HUMMEL* at the University of Hamburg as well as on HLRN-III (<http://www.hlrn.de>) under project ID hhp00022. BK further gratefully acknowledges the Gauss Centre for Supercomputing e.V. (www.gauss-centre.eu) for funding this project (project ID pr92pu) by providing computing time on the GCS Supercomputer SuperMUC at Leibniz Supercomputing Centre (LRZ, <http://www.lrz.de>).

REFERENCES

- André P. et al., 2010, *A&A*, 518, L102
 André P., Di Francesco J., Ward-Thompson D., Inutsuka S.-I., Pudritz R. E., Pineda J. E., 2014, in Beuther H., Klessen R. S., Dullemond C. P., Henning T., eds, *Protostars and Planets VI*. Univ. Arizona Press, Tucson, p. 27
 Arzoumanian D. et al., 2011, *A&A*, 529, L6
 Bally J., 1989, in Reipurth B., ed., *European Southern Observatory Conference and Workshop Proceedings Vol. 33, The Structure and Kinematics of Star Forming clouds*. European Southern Observatory, Garching bei München, p. 1
 Barnard E. E., 1905, *PLATE 41*, In *Aquila, North-west of Altair*
 Barnes A. T., Kong S., Tan J. C., Henshaw J. D., Caselli P., Jiménez-Serra I., Fontani F., 2016, *MNRAS*, 458, 1990
 Boekholt T. C. N., Stutz A. M., Fellhauer M., Schleicher D. R. G., Matus Carrillo D. R., 2017, *MNRAS*, 471, 3590
 Bonnell I. A., Bate M. R., Clarke C. J., Pringle J. E., 2001, *MNRAS*, 323, 785
 Bouchut F., Klingenberg C., Waagan K., 2010, *Numer. Math.*, 115, 647
 Bovino S., Grassi T., Schleicher D. R. G., Caselli P., 2017, *ApJ*, 849, L25
 Brünken S. et al., 2014, *Nature*, 516, 219

Burkert A., Hartmann L., 2004, *ApJ*, 616, 288
 Caselli P., Walmsley C. M., Zucconi A., Tafalla M., Dore L., Myers P. C., 2002, *ApJ*, 565, 344
 Chandrasekhar S., Fermi E., 1953, *ApJ*, 118, 116
 Chen H.-R., Liu S.-Y., Su Y.-N., Wang M.-Y., 2011, *ApJ*, 743, 196
 Clarke S. D., Whitworth A. P., 2015, *MNRAS*, 449, 1819
 Clarke S. D., Whitworth A. P., Duarte-Cabral A., Hubber D. A., 2017, *MNRAS*, 468, 2489
 Crutcher R. M., 2012, *ARA&A*, 50, 29
 Crutcher R. M., Wandelt B., Heiles C., Falgarone E., Troland T. H., 2010, *ApJ*, 725, 466
 Dubey A. et al., 2008, in Pogorelov N. V., Audit E., Zank G. P., eds, ASP Conf. Ser. Vol. 385, Numerical Modelling of Space Plasma Flows. Astron. Soc. Pac., San Francisco, p. 145
 Elmegreen B. G., Scalo J., 2004, *ARA&A*, 42, 211
 Federrath C., Banerjee R., Clark P. C., Klessen R. S., 2010, *ApJ*, 713, 269
 Fiege J. D., Pudritz R. E., 2000, *MNRAS*, 311, 85
 Flower D. R., Pineau Des Forêts G., Walmsley C. M., 2006, *A&A*, 449, 621
 Fontani F. et al., 2011, *A&A*, 529, L7
 Fryxell B. et al., 2000, *ApJS*, 131, 273
 Giannetti A. et al., 2014, *A&A*, 570, A65
 Goodson M. D., Kong S., Tan J. C., Heitsch F., Caselli P., 2016, *ApJ*, 833, 274
 Grassi T., Bovino S., Schleicher D. R. G., Prieto J., Seifried D., Simoncini E., Gianturco F. A., 2014, *MNRAS*, 439, 2386
 Hacar A., Tafalla M., 2011, *A&A*, 533, A34
 Hacar A., Tafalla M., Kauffmann J., Kovács A., 2013, *A&A*, 554, A55
 Hanawa T., Tomisaka K., 2015, *ApJ*, 801, 11
 Heiles C., 1987, in Morfill G. E., Scholer M., eds, NATO ASIC Proc. 210: Physical Processes in Interstellar Clouds Interstellar Magnetic Fields. D. Reidel Publ. Co., Dordrecht, p. 429
 Heiles C., 1997, *ApJS*, 111, 245
 Hernandez A. K., Tan J. C., Caselli P., Butler M. J., Jiménez-Serra I., Fontani F., Barnes P., 2011, *ApJ*, 738, 11
 Hocuk S., Cazaux S., Spaans M., 2014, *MNRAS*, 438, L56
 Juvela M. et al., 2012, *A&A*, 541, A12
 Kauffmann J., Pillai T., Goldsmith P. F., 2013, *ApJ*, 779, 185
 Kirk H. et al., 2017, *ApJ*, 846, 144
 Kong S., Caselli P., Tan J. C., Wakelam V., Sipilä O., 2015, *ApJ*, 804, 98
 Körtgen B., Bovino S., Schleicher D. R. G., Giannetti A., Banerjee R., 2017, *MNRAS*, 469, 2602
 Lackington M., Fuller G. A., Pineda J. E., Garay G., Peretto N., Traficante A., 2016, *MNRAS*, 455, 806
 Leurini S., Pillai T., Stanke T., Wyrowski F., Testi L., Schuller F., Menten K. M., Thorwirth S., 2011, *A&A*, 533, A85
 Li H.-b., Fang M., Henning T., Kainulainen J., 2013, *MNRAS*, 436, 3707
 Li H.-B., Jiang H., Fan X., Gu Q., Zhang Y., 2017, *Nat. Astron.*, 1, 0158
 Lukat G., Banerjee R., 2016, *New Astron.*, 45, 14
 Mac Low M.-M., Klessen R. S., 2004, *Rev. Modern Phys.*, 76, 125
 Majumdar L. et al., 2017, *MNRAS*, 466, 4470
 Matsumoto T., Nakamura F., Hanawa T., 1994, *PASJ*, 46, 243
 McKee C. F., Ostriker E. C., 2007, *ARA&A*, 45, 565
 McKee C. F., Tan J. C., 2003, *ApJ*, 585, 850
 Molinari S. et al., 2010, *A&A*, 518, L100
 Myers P. C., 2009, *ApJ*, 700, 1609
 Nagasawa M., 1987, *Prog. Theor. Phys.*, 77, 635
 Nakamura F., Hanawa T., Nakano T., 1993, *PASJ*, 45, 551
 Ostriker J., 1964, *ApJ*, 140, 1056
 Pagani L. et al., 2009, *A&A*, 494, 623
 Pagani L., Roueff E., Lesaffre P., 2011a, *ApJ*, 739, L35
 Pagani L., Roueff E., Lesaffre P., 2011b, *ApJ*, 739, L35
 Pagani L., Lesaffre P., Jorfi M., Honvault P., González-Lezana T., Faure A., 2013, *A&A*, 551, A38
 Pattle K. et al., 2017, *ApJ*, 846, 122
 Pillai T., Caselli P., Kauffmann J., Zhang Q., Thompson M. A., Lis D. C., 2012, *ApJ*, 751, 135
 Schleicher D. R. G., Stutz A., 2018, *MNRAS*, 475, 121
 Schmidt W., Collins D. C., Kritsuk A. G., 2013, *MNRAS*, 431, 3196

Seifried D., Walch S., 2015, *MNRAS*, 452, 2410
 Seifried D., Walch S., 2016, *MNRAS*, 459, L11
 Seifried D., Sánchez-Monge Á., Suri S., Walch S., 2017, *MNRAS*, 467, 4467
 Sipilä O., Caselli P., 2018, *A&A*, in press
 Stutz A. M., Gould A., 2016, *A&A*, 590, A2
 Toalá J. A., Vázquez-Semadeni E., Gómez G. C., 2012, *ApJ*, 744, 190
 Toci C., Galli D., 2015, *MNRAS*, 446, 2118
 Tomisaka K., 2014, *ApJ*, 785, 24
 Truelove J. K., Klein R. I., McKee C. F., Holliman J. H., II, Howell L. H., Greenough J. A., 1997, *ApJ*, 489, L179
 Vastel C. et al., 2012, *A&A*, 547, A33
 Waagan K., Federrath C., Klingenberg C., 2011, *J. Comput. Phys.*, 230, 3331
 Walmsley C. M., Flower D. R., Pineau des Forêts G., 2004, *A&A*, 418, 1035

APPENDIX: VARYING INITIAL CONDITIONS

A major source of uncertainty in our model are the cosmic ray flux, ζ , the initial ortho-to-para ratio of H_2 as well as the abundances of certain chemical species. The cosmic ray flux is currently known to be on average $\zeta \sim 10^{-17} \text{ s}^{-1}$, but the scatter is almost an order of magnitude or larger. The ortho-to-para ratio of H_2 is known to decrease with time, but tight constraints on the concrete value in filaments and cores are still missing, because of the observational difficulty to assess the para state with ground-based telescopes. For these reasons, we here briefly consider the evolution of the average deuteration fraction for different initial conditions such as varying cosmic ray flux, varying ortho-to-para ratio, different gas temperature or different initial abundances of certain ions.

The results for the different initial conditions are shown in Fig. A1. The fiducial case is depicted by the solid red line with a cosmic ray flux of $\zeta = 1.3 \times 10^{-17} \text{ s}^{-1}$. In agreement with the parameter study by Kong et al. (2015), varying the cosmic ray flux by a factor of 5 has a strong impact on the time evolution of the average deuterium fraction within the filament. Specifically, an in-

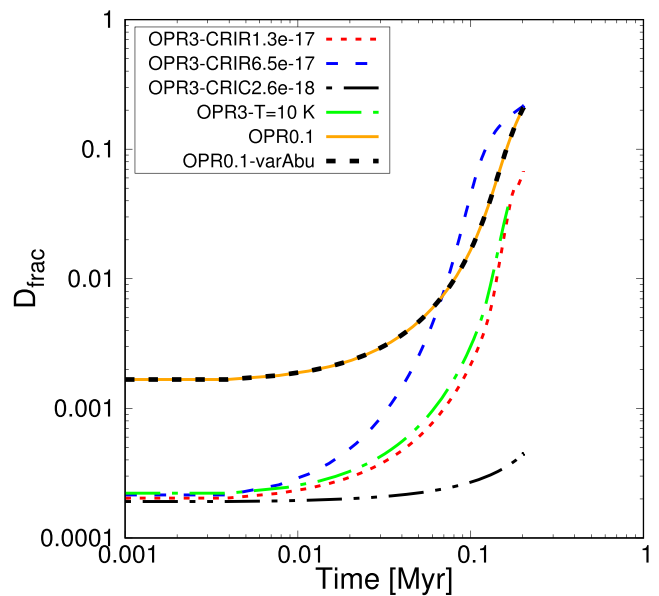


Figure A1. Time evolution of the average deuteration fraction for different initial conditions. It is clear from these results that the ortho-to-para ratio as well as the cosmic ray flux have the strongest influence on the evolution of the deuterium fraction. Variations in the temperature or the initial ion abundances only yield minor deviations from the respective reference case.

Table A1. Initial mass fractions of H₂ and the relevant ion species in our simulations. OPR stands for ortho-to-para ratio of H₂.

Species	Fiducial, OPR = 3	Control, OPR = 0.1	Control, OPR = 0.1, varying abundances
p-H ₂	0.17858	0.64939	0.64939
o-H ₂	0.53574	0.064939	0.064939
H ⁺	7.14×10^{-13}	7.14×10^{-13}	1.25×10^{-09}
p-H ₃ ⁺	2.14×10^{-12}	2.14×10^{-12}	1.28×10^{-09}
o-H ₃ ⁺	2.14×10^{-12}	2.14×10^{-12}	3.84×10^{-09}
p-H ₂ D ⁺	1.00×10^{-20}	1.00×10^{-20}	3.69×10^{-11}
o-H ₂ D ⁺	1.00×10^{-20}	1.00×10^{-20}	2.96×10^{-10}
D ₂ H ⁺	1.00×10^{-20}	1.00×10^{-20}	5.21×10^{-11}
D ₃ ⁺	1.00×10^{-20}	1.00×10^{-20}	1.99×10^{-11}

creased ζ results in a far higher deuterium fraction, by up to a factor of ~ 2 , at the same temporal stage compared to the fiducial run. Furthermore, the increased flux causes the fraction of deuterium to increase sooner due to the enhanced formation of H₃⁺ and the subsequent formation of H₂D⁺. If the cosmic ray flux is reduced, the resulting deuteration fraction is drastically reduced by up to 2 orders of magnitude.

In a next step, the gas temperature was varied from $T = 15$ K down to $T = 10$ K with the other parameters being the same. The resultant evolution is shown as the green curve in Fig. A1. Except for some small deviation, the time evolution appears to be independent of the gas temperature. As stated in Kong et al. (2015), this is to

be expected as at such low temperatures, the reactions including ortho-H₂ are effectively suppressed and the chemical evolution is governed by temperature independent reactions.

Furthermore, we reduce the initial ortho-to-para ratio of H₂ to a value of 0.1. The time evolution of this simulation is shown as the yellow solid line. As expected, the greatly reduced amount of ortho-H₂ favours the formation of H₂D⁺, resulting in an enhanced deuterium fraction from early times on. At late times, $t \sim 200$ kyr, the average deuterium fraction is about a factor of 2 higher relative to the fiducial case with an initial ortho-to-para ratio of 3.

When the filament is formed during the evolution of the parental molecular cloud, also the abundance of the chemical species is increased. For this reason, we carried out a control simulation with an initial ortho-to-para ratio of H₂ of 0.1 and increased abundances of certain ion species (see Table A1), where the latter are taken from the free-fall model of Flower et al. (2006). The time evolution of this run is shown as the black dashed line in Fig. A1. The variation in the average deuterium fraction is negligibly small compared to the run, where only the ortho-to-para ratio was varied. This indicates that the initial abundances of ions do not influence the resultant deuterium fraction. To summarize this parameter exploration, we see that only the ortho-to-para ratio of H₂ and the cosmic ray flux significantly impact the evolution of the deuterium fraction, in agreement with previous lower dimensional studies by Flower et al. (2006) and Kong et al. (2015).

This paper has been typeset from a $\text{\TeX}/\text{\LaTeX}$ file prepared by the author.